

*Schmisseur*

AFRL-SR-AR-TR-04

19  
or  
of

0227

REPORT DOCUMENTATION PAGE		
<p>Public reporting burden for this collection of information is estimated to average 1 hour per response, including the time for reviewing the data needed, and completing and reviewing this collection of information. Send comments regarding this burden estimate or any reducing this burden to Washington Headquarters Services, Directorate for Information Operations and Reports, 1215 Jefferson Davis Highway, Suite 1204, Arlington, VA 22202-4302, and to the Office of Management and Budget, Paperwork Reduction Project (0704-0188), Washington, DC 20503.</p>		
1. AGENCY USE ONLY (Leave blank)	2. REPORT DATE	3. REPORT TYPE AND DATES COVERED
	December 30 2003	Final Technical Report April 1, 2001 – December 31, 2003
4. TITLE AND SUBTITLE		5. FUNDING NUMBERS
3D Particle Tracking Velocimetry of Transverse Injection in Supersonic Flow		49620-01-1-0111
6. AUTHOR(S)		
H. G. Hornung (PI), N. Ponchaut, C. Mouton		
7. PERFORMING ORGANIZATION NAME(S) AND ADDRESS(ES)		8. PERFORMING ORGANIZATION REPORT NUMBER
Graduate Aeronautical Laboratories California Institute of Technology		1200 E. California Blvd. Pasadena, CA 91125
9. SPONSORING / MONITORING AGENCY NAME(S) AND ADDRESS(ES)		10. SPONSORING / MONITORING AGENCY REPORT NUMBER
Air Force Office of Scientific Research		4015 Wilson Blvd., Room 713, Arlington, VA 22203-1954
11. SUPPLEMENTARY NOTES		
12a. DISTRIBUTION / AVAILABILITY STATEMENT		12b. DISTRIBUTION CODE
Approved for general release, distribution is unlimited		20040426 062
13. ABSTRACT (Maximum 200 Words)		
<p>The supersonic Ludwieg Tube at the Graduate Aeronautical Laboratories of the California Institute of Technology was completed and taken into operation. A smaller Ludwieg Tube with the purpose of providing a transverse jet in the main flow was constructed and taken into operation, thus completing a compact, inexpensive supersonic flow/injection facility. The implementation of three-component, three-dimensional particle image velocimetry in supersonic air flows from the instrument existing for low speed water flows at the time of inception of the program required a much greater development effort than had been anticipated at the outset. Major redesign of the hardware and new software development as well as experimentation with particle-generating systems produced an instrument that is now able to fulfill the tasks demanded of it for the project with good accuracy and spatial resolution. Velocities parallel to the camera face can be measured to an accuracy of 0.25% and the component normal to the camera face to 2.5%.</p>		
14. SUBJECT TERMS		15. NUMBER OF PAGES
3D flow field, particle tracking velocimetry, supersonic flow		33
		16. PRICE CODE
17. SECURITY CLASSIFICATION OF REPORT	18. SECURITY CLASSIFICATION OF THIS PAGE	19. SECURITY CLASSIFICATION OF ABSTRACT
Unclassified	Unclassified	Unclassified
20. LIMITATION OF ABSTRACT		
U/L		
NSN 7540-01-280-5500		

RECEIVED JAN 05 2004

**3D PARTICLE TRACKING VELOCIMETRY ON  
TRANSVERSE INJECTION IN SUPERSONIC FLOW**

H. G. Hornung (PI), N. Ponchaut, C. Mouton

Graduate Aeropnautical Laboratories  
California Institute of Technology  
Pasadena, CA 91125

December 30, 2003

**Final Technical Report, Grant No. 49620-01-1-0111**

Approved for public release; distribution is unlimited

Prepared for  
**AIR FORCE OFFICE OF SCIENTIFIC RESEARCH**  
4015 Wilson Blvd, Room 713, Arlington VA 22203-1954

# Contents

<b>1</b>	<b>Introduction</b>	<b>3</b>
<b>2</b>	<b>The supersonic Ludwieg Tube</b>	<b>4</b>
2.1	LT nozzle calibration . . . . .	5
2.2	The injection system . . . . .	6
<b>3</b>	<b>The three-dimensional particle tracking velocimetry system</b>	<b>8</b>
3.1	Introduction . . . . .	8
3.2	Principle . . . . .	9
3.2.1	3DPTV Design . . . . .	10
3.2.2	Varying Media Influence . . . . .	14
3.2.3	Current Camera . . . . .	14
3.3	Data Processing Program . . . . .	15
3.4	Error Analysis . . . . .	15
3.4.1	Index of Refraction . . . . .	15
3.4.2	Tracking Error . . . . .	17
3.5	Results . . . . .	19
3.5.1	Synthetic Images . . . . .	19
3.5.2	Moving Plate . . . . .	20
3.5.3	3D Solid Imaging . . . . .	27
3.5.4	Sonic Jet Injection . . . . .	27
3.6	Conclusions . . . . .	29
<b>4</b>	<b>General Conclusions</b>	<b>30</b>
<b>5</b>	<b>Personnel associated with the research</b>	<b>30</b>

6	Publications resulting from the work	30
7	Honors and awards	31
8	Acknowledgments	31

# 1 Introduction

There are two main reasons for transverse gas injection into supersonic flows. One is to mix fuel into a supersonic air stream for supersonic-combustion ram jet propulsion, where the emphasis is on quality of mixing. The other is to cause a reaction force on a vehicle traveling at supersonic speed, or in a supersonic nozzle for thrust-vector control, where the emphasis is on effectiveness and undetectability of vehicle control. In both cases good design depends crucially on the capability to compute, and thus to predict, the associated complex turbulent flow field.

At the outset of the program, the GALCIT supersonic Ludwieg Tube (LT) was within six months of being completed. This facility provides a flow at Mach number 2.3 in a test section of  $200 \times 200$  mm cross section for a duration of 80 ms. It is very inexpensive to operate. A secondary Ludwieg Tube for synchronized gas injection into the supersonic flow was under development.

At the same time, the development of digital defocusing particle imaging velocimetry (DDPIV) by the Gharib group at GALCIT for use in low speed water flows had made it possible to obtain three-dimensional, three-component, instantaneous measurements of a complete velocity field. The combination a suitable variant of this tool for supersonic flow with the LT promised to make the acquisition of such flow fields highly productive and inexpensive. Comparing the method with regular or even Stereo DPIV, where the data from one run would be a velocity vector field in just one plane, so that many runs would be required to get a velocity field on a three-dimensional grid (and which therefore would not be temporally correlated), the productivity is increased by a factor of 20 or so, and the value of the temporal correlation of the vector field is huge. With an expected turnaround frequency of the LT of 6 runs per day, and at an operating cost of \$ 400 per day, this was a very attractive proposition.

More sophisticated turbulence computations are being made accessible by rapid developments in computational power and data storage of modern machines every year. More sophisticated turbulence models are being developed at the same time. Computational fluid dynamicists are asking for more complete and more highly resolved data than are currently available for transverse injection into supersonic flow.

The motivations for the work was thus to investigate the flow field of transverse injection into a supersonic flow with fine spatial resolution of the instantaneous, three-dimensional, three-component velocity field, the productivity of the method permitting coverage of large ranges of the parameter space.

In order to be able to develop the instrument, a separate proposal for a DURIP Grant was made. This was successful, and the instrument was built in its first form under the DURIP Grant. It rapidly became clear during further development and calibration of the instrument, that the step from low speed water flows to supersonic flows at Mach 2.3 in air involves major development. The original statement of work (see Appendix A) thus turned

out to be much too ambitious. In the three-year program we can therefore only claim to have achieved the development of the instrument to the stage where it can be applied with success in supersonic air flows. In order to achieve this, the instrument had to be significantly modified, and entirely new software had to be developed. The major part of this final report describes this work.

Before getting to that part, the next section describes the Ludwieg Tube and the secondary Ludwieg Tube.

## 2 The supersonic Ludwieg Tube

A Ludwieg Tube consists of a long tube, filled initially with high-pressure gas, that is connected via a nozzle and test section to an evacuated dump tank. The dump tank and test section are separated by a diaphragm which is ruptured to initiate the flow. During the time it takes for the expansion wave generated by the diaphragm rupture to propagate to the far end of the Ludwieg tube and back, the flow into the nozzle is perfectly steady and uniform except for the boundary layer on the tube wall, which grows with time and becomes turbulent after a certain time.

A donation from the John and Anna Wild estate enabled us to design and build a Ludwieg Tube to replace the small continuous-flow supersonic tunnel that was scrapped as part of the Guggenheim building rehabilitation. The LT has been operational since 2001. The total cost of the facility is \$ 500,000. The first nozzle of the LT is designed for a Mach number of 2.3 with a test section cross section of  $200 \times 200$  mm. The minimum free-stream viscous length scale  $\nu_\infty/U_\infty = 10$  nm, giving a maximum Reynolds number on a length of 200 mm of  $20 \times 10^6$ . The tube has a diameter of 300 mm and a length of 17 m honed to a smooth finish. This provides a theoretical test duration of 100 ms. The starting process takes approximately 20 ms, so that the clean test duration is 80 ms, or 200 flow times for a 200 mm model. The short test time is the reason for the inexpensive operation of the LT. A perspective view of the facility is shown in Fig. 1.

A particular feature of the GALCIT LT is the method by which the tube boundary layer is removed. From experimental results obtained by Chun (private communication) it has become clear that the growth of the boundary layer in a LT and the transition to turbulent flow in this boundary layer can provide serious impairment of the flow quality, and this makes it unattractive to extend the tube beyond approximately 40 diameters. Even then, it is desirable to suck off the tube-wall boundary layer. This is done by providing a flow path, parallel to that through the nozzle, through an annular throat just upstream of the contraction, through a manifold and four tubes to the space upstream of the diaphragm, see Fig. 2. So, when the diaphragm is ruptured, an expansion wave passes both through the test section and nozzle into the tube, and through the tubes, manifold and annular throat into the tube. This sets up both flows. As the tube-wall boundary layer grows, the rounded nose on the inside of the annular throat permits the stagnation point to move without causing

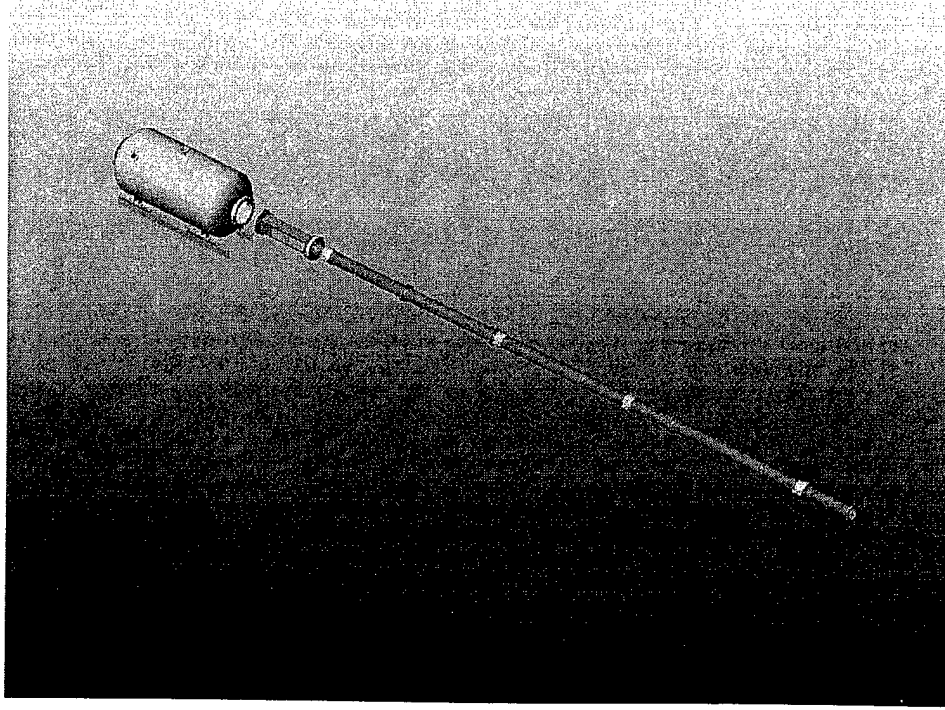


Figure 1: Perspective view of Ludwieg tube, nozzle, test section and dump tank

separation. A computation of this flow indicates that this method of boundary-layer removal starts the flow successfully. The region around the annular throat is instrumented with pressure transducers in order to monitor the performance of the removal system. During the calibration of the LT, these transducers showed that the flow downstream of the annular throat is supersonic, thus ensuring that no noise can enter the main flow from the suction manifold.

## 2.1 LT nozzle calibration

The two-dimensional Mach 2.3 nozzle was designed by J. J. Korte of NASA Langley RC. The complete nozzle flow was calibrated [1] by using the Mach-wave method in which weak disturbances are generated at opposite nozzle walls by sticking strips of thin adhesive tape to the walls. The weak Mach waves generated by the tapes can be visualized by the schlieren technique. The angles of the intersecting Mach waves give the local Mach number and flow direction. A composite view of the schlieren images is shown in Fig. 3, and the resulting Mach number distribution is compared with the design curve in Fig. 4

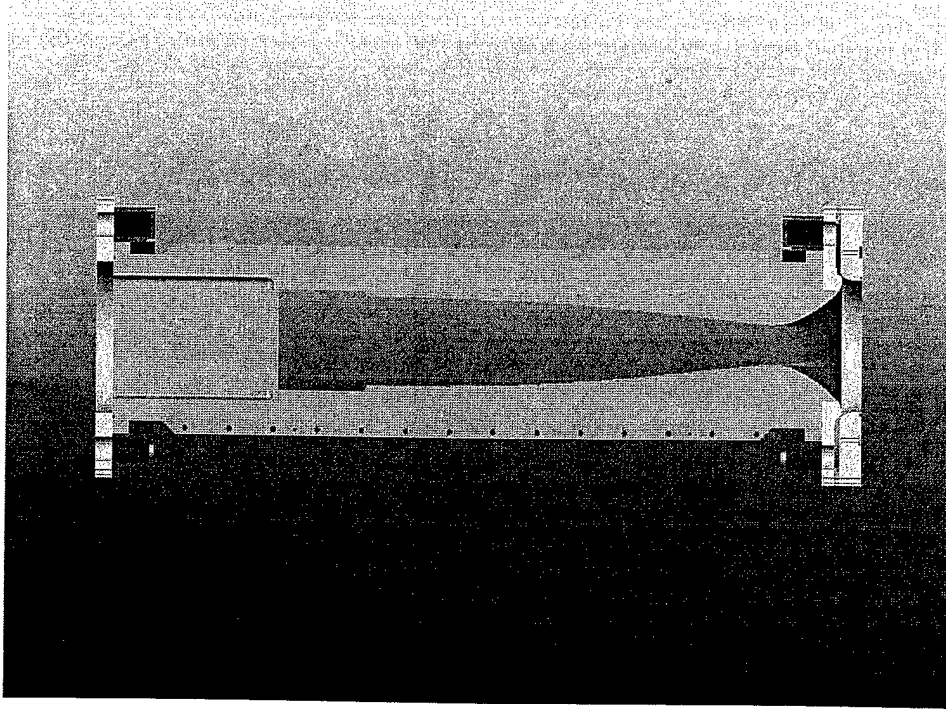


Figure 2: Longitudinal section through nozzle and test section. To the right, this is joined by the 17 m long 300 mm diameter tube, and to the left by the diaphragm rupture system and dump tank. The light blue and yellow parts at the right form the annular throat of the boundary-layer removal system. The magenta part shows the transition from the circular section to the rectangular throat. The four tubes connecting the two green manifolds of the boundary-layer removal system are not shown.

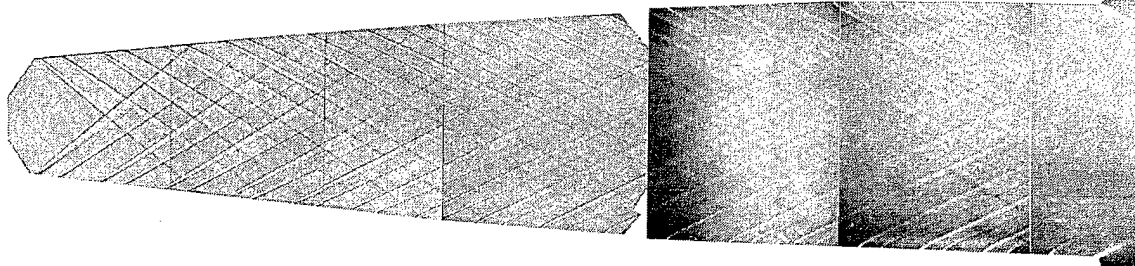


Figure 3: Composite schlieren picture of the whole nozzle flow, made up of seven separate images.

## 2.2 The injection system

In order to be able to control the state of the boundary layer on the surface from which the gas injection takes place, a flat plate is constructed that is located parallel to and a small distance below the test section roof. This enables the tunnel-wall boundary layer to be diverted. The injection jet is generated with a separate small injection Ludwieg Tube (ILT) of 50 mm internal diameter and 10 m length. This feeds the injection nozzle via a

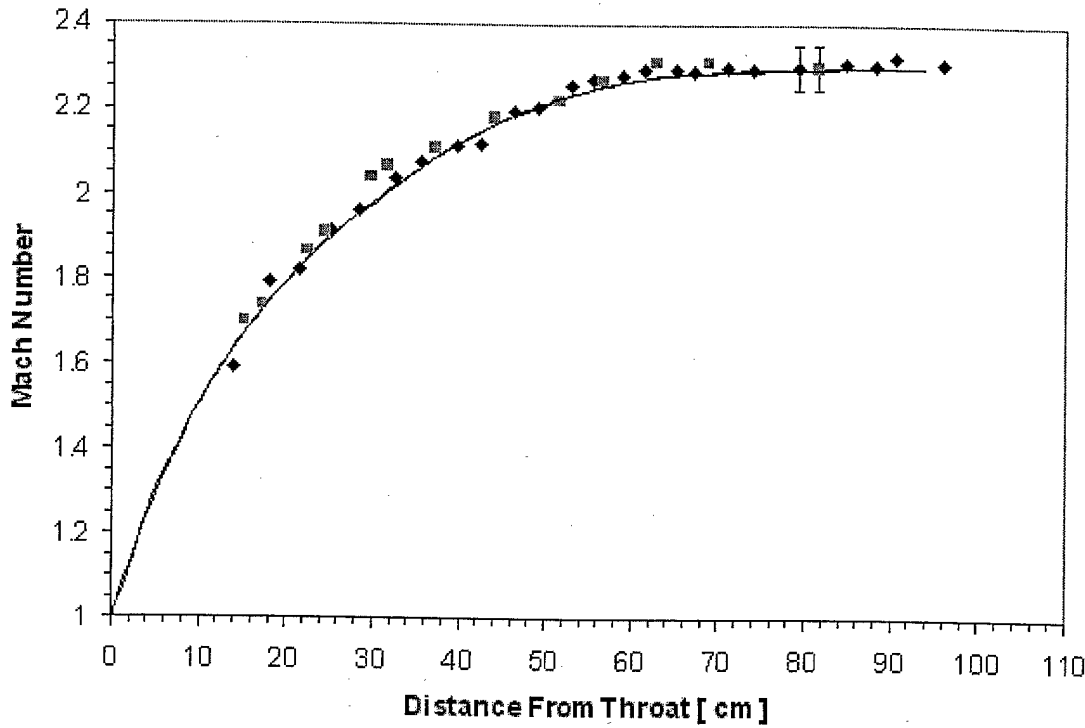


Figure 4: Mach number distribution obtained from measurements of the intersection angles of the waves in Fig 3. The diamonds represent measurements of the intersection of the weak shocks. The squares represent measurements from intersections of the leading characteristics of the trailing expansion waves. The full line is the centerline Mach number distribution obtained by J. J. Korte in his design of this nozzle, which takes account of the boundary layer displacement thickness.

mylar diaphragm that is ruptured by discharging a capacitor through a tungsten wire that is clamped onto the mylar diaphragm. The local heating of the mylar diaphragm causes a disk-like piece of the diaphragm to be cut out. This permits accurate synchronization of the injection flow with the main flow. The maximum injection nozzle exit diameter is 12 mm. This large diameter makes the size of the flow field of interest in the longitudinal vertical plane approximately  $150 \times 200$  mm. The maximum jet Reynolds number is  $4 \times 10^6$ .

The injection is timed to start immediately after the starting process of the main nozzle flow is over and the boundary-layer removal system has reached steady state. This will be no later than 20 ms after main diaphragm rupture. The flow duration of the ILT is approximately 60 ms.

A schlieren image of the flow with the ILT in synchronized operation with the LT is shown in Fig. 5.

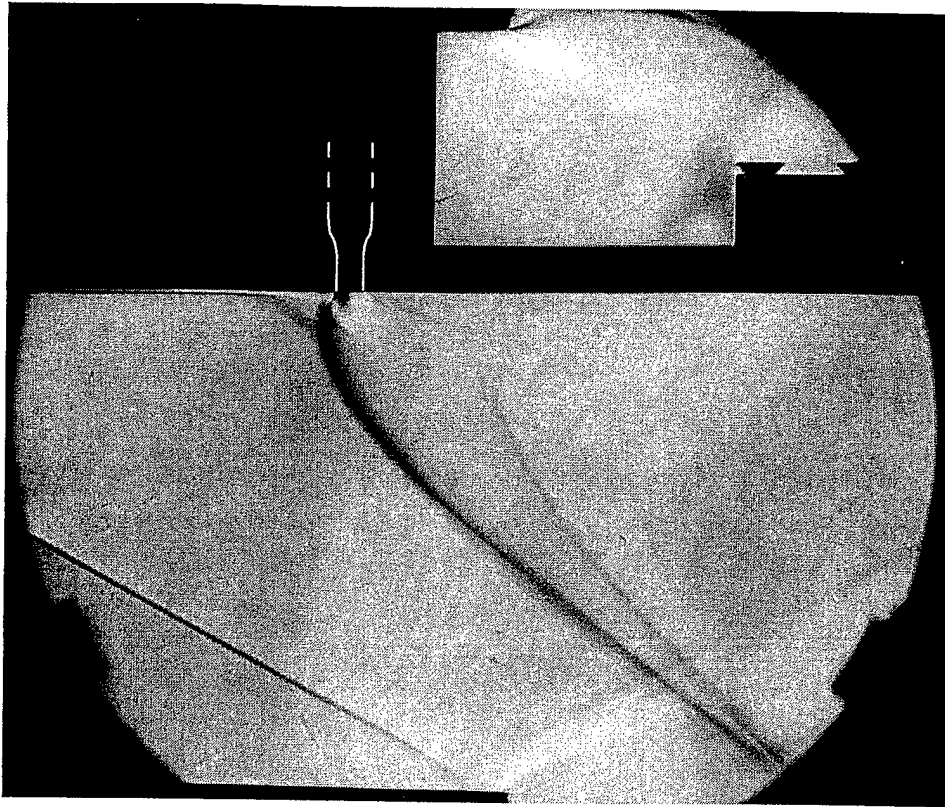


Figure 5: Schlieren image of the jet in cross flow. The exposure time is too long to resolve the turbulent structure in this image

### 3 The three-dimensional particle tracking velocimetry system

#### 3.1 Introduction

During the last few decades, flow experiments where three-dimensional features are of interest have become more common. This evolution brings the need for a full three-component, three-dimensional velocity field measurement technique. For that purpose, some researchers have developed methods using a single camera [2] or several cameras (generally 3 or 4 using the epipolar technique) [3, 4, 5]. Of particular interest is the work done by F. Pereira *et al.* [4, 6] in developing a digital defocusing particle image velocimetry (DDPIV) system. Their system uses three individual CCDs placed at the vertices of an equilateral triangle, with all three cameras having overlapping fields of view. The test section can be placed anywhere in this overlap region. Every particle in the test section will be projected onto each CCD. If the CCD images are overlaid, the three images of a particle will be located at the three corners of a near-equilateral triangle. By performing triangulation, the three-dimensional position of a particle can be calculated. Sub-pixel accuracy of a particle image location is obtained by having the images unfocused, which drastically improves the overall

resolution of the system. This design was patented by Gharib *et al.*, and is assigned to the California Institute of Technology (U.S. Patent #6,278,947). Currently, this technology is being developed for commercial use by VioSense Corporation of Pasadena, California. F. Pereira *et al.* also developed a sophisticated software toolkit which allows users to analyze the raw CCD images and transform them into a three-dimensional velocity field. The DDPIV system has been applied to bubbly flows.

The current authors first revisited some of the design choices made by F. Pereira *et al.*, and improved upon some of them. Also, since the source-code of F. Pereira *et al.* is proprietary, a completely new software package was developed and is significantly different from the DDPIV software package. The current authors will investigate supersonic air flows, whereas F. Pereira *et al.* investigated low-speed water flows. Of course, the software of both F. Pereira *et al.* and the current authors share some of the same theoretical foundation; however, much of the new software is significantly different and substantially improved. These improvements provide increased accuracy of results. F. Pereira *et al.* chose to use a statistical calculation for the velocity field; whereas, the current authors pursue direct particle tracking. The system developed by the current authors is referred to as three dimensional particle triangulation velocimetry (3DPTV).

## 3.2 Principle

Both the hardware setup of F. Pereira *et al.* for DDPIV and the hardware setup of 3DPTV consist of a camera comprising three separate CCDs, which all view the same test volume from different angles. The front plate of the camera consists of a mask, three lenses, and three apertures, behind each of which there is a CCD. The need for more than two CCDs and suggestion that with three cameras an equilateral triangle is the optimum configuration is discussed by Maas *et al.* [3]. In the DDPIV setup, the center of a target plate is focused onto the center of each CCD. Figure 6 shows this for one of the CCDs. In this arrangement, the image of the test volume does not fill the frame of the CCD. In order to make full use of all the pixels of the CCD, 3DPTV uses offsets, in which the CCDs are moved away from the lens and away from the camera axis as shown in Figure 6. Of course, full use of the CCDs could also be achieved by placing the target plate in the test volume, but this has some disadvantages, as is discussed later. The image of each point on the target plate will appear at the same place on each of the three CCDs, once the correction for the offsets has been made.

In practice it is impossible to place the CCDs in their exact theoretical locations; therefore, careful alignment followed by calibration is required. In order to do this, a well designed target is needed in addition to calibration software. For this purpose the authors designed a target with 100 equally spaced dots per square inch. With this target placed at the target plane, the CCDs should be placed such as to focus and match each of the three images as well as possible. The calibration software compares the measured and known dot locations, and then creates a mapping to correct for errors in CCD placement as well as lens aberrations

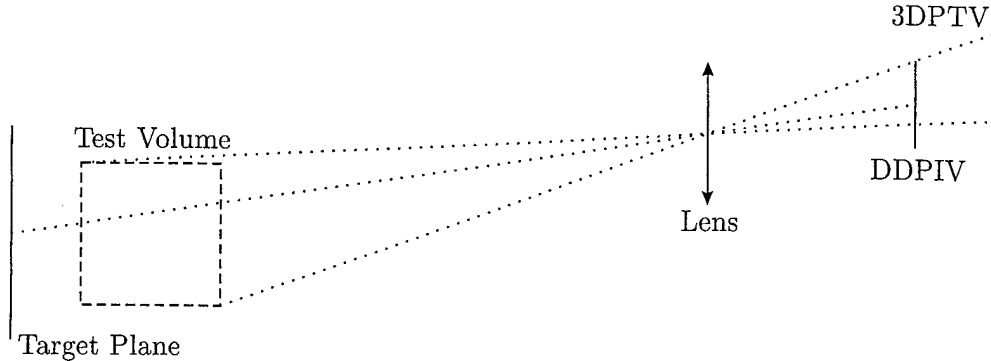


Figure 6: Maximum CCD utilization using offsets.

and other effects.

Once the camera has been aligned and calibrated, the images of a particle that does not lie on the target plane will appear at the vertices of an equilateral triangle on the overlaid CCD images. The formation of triangles on the overlaid images is shown in Figure 7. Clearly, it is only a matter of ray tracing to transform a triangle on the CCDs to a particle location.

Particle tracking is conceptually a simple task. Once all of the three dimensional positions are known, all that is required to determine the three components of the velocity of the particles is to find corresponding particles in two successive frames separated by a known short time interval.

### 3.2.1 3DPTV Design

The design of the 3DPTV system involves many related parameters. Choosing the best parameters for a set of particular requirements is truly a design exercise. The governing equations used in this design are now presented. A key assumption in the design is that the medium surrounding the camera has a constant refractive index. The fact that this assumption is not true means that the system will be used in an off-design regime; however, for the current parameters this leads to only a very small deviation from the optimum.

#### *Blur Radius Estimation*

The blur radius has a big influence on the results one can obtain with both DDPIV and 3DPTV. A sufficiently large blur radius is required to get sub-pixel accuracy; however, the larger the blur radius, the more often particle images will overlap, thereby making it more difficult to process the data. An estimate of the blur radius can be calculated by considering the quasi-one-dimensional problem of a single lens of focal length  $f$  and a single CCD as shown in Figure 8. The distance between the lens and CCD, in the  $z$ -direction, is  $d_C$  and the lens has an aperture of radius  $r_p$ . The setup was constructed so that a particle placed at a distance  $L$  from the camera will be focused on the CCD. If a particle is at a distance  $z$ , it

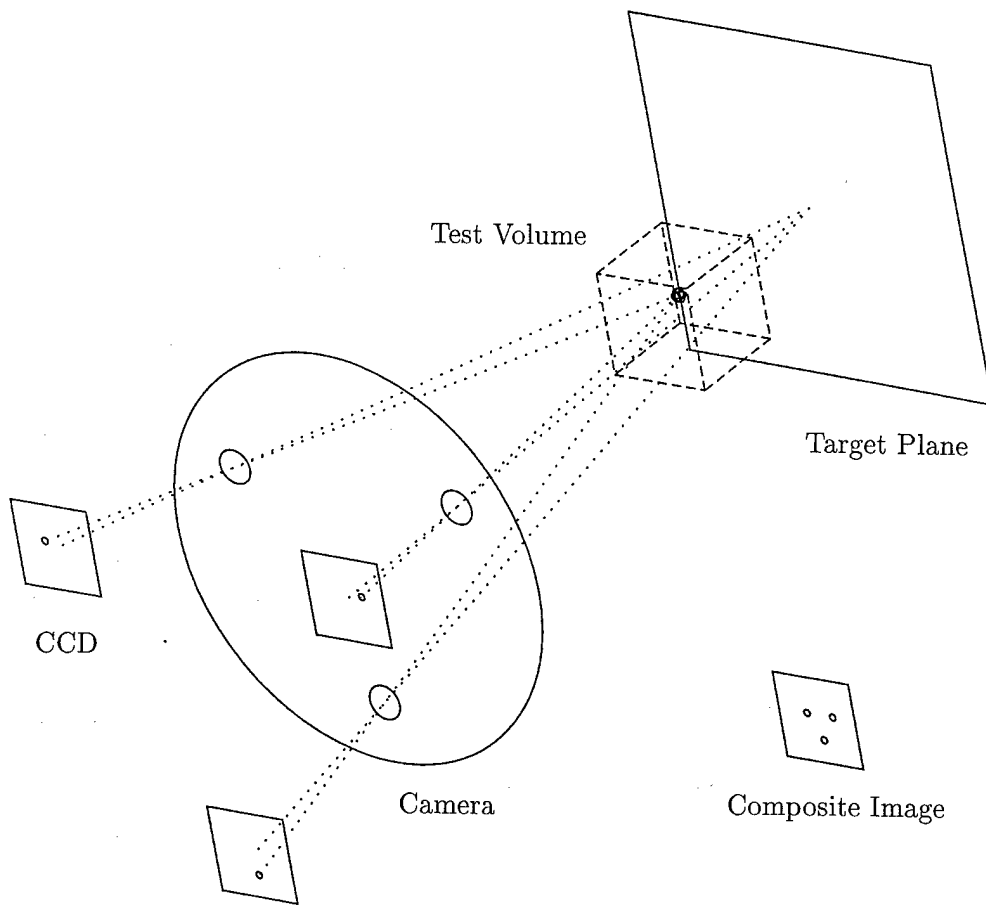


Figure 7: Projection of a particle onto the CCDs, with appropriate offsets taken into account.

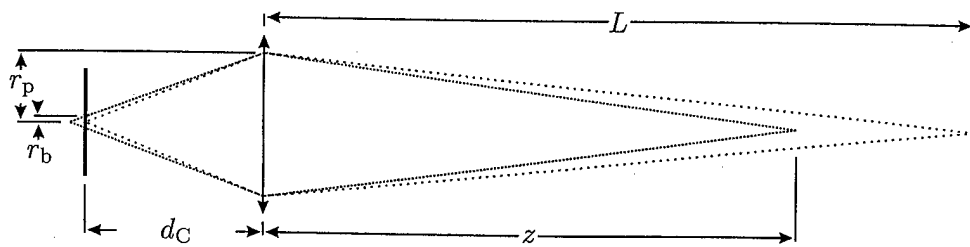


Figure 8: Quasi 1-D blur radius evaluation.

will be focused away from the CCD, at a distance  $fz/(z - f)$ . Geometric relations lead to an estimation of the blur radius,  $r_b$ ,

$$r_b = r_p \frac{\frac{L}{z} - 1}{\frac{L}{f} - 1}.$$

The rate of change of the blur radius to a movement in  $z$  is

$$\frac{dr_b}{dz} = -r_p \frac{fL}{(L - f)z^2}.$$

The data processing program has to find the centroids of all the Gaussian intensity distributions of the blurred particle images. The program does not know the blur radius of a particle image *a priori* since the particle location is unknown. The performance of the program is improved by operating with a small range of blur radii. The value of the average blur radius and range of blur radii are parameters that must be considered when choosing both  $L$  and  $f$ . One should also note that a nonzero blur radius is required to achieve sub-pixel accuracy; therefore, the focal plane can not be located within the test volume.

### *Alignment*

As explained before, the camera is composed of three CCDs placed at the vertices of an equilateral triangle. Let the coordinates of the center of the  $i^{\text{th}}$  CCD be  $\mathbf{P}_i^c$ . Each of the CCDs views the test volume through its own lens, of focal length  $f$ , which is located at  $\mathbf{P}_i^l$ . An object placed at the focal distance of the camera,  $L$ , will look exactly the same on each CCD, after appropriate offsets have been taken into account, and will be focused. Therefore, the distance in the  $z$ -direction, between the CCD and the optical center of the lens,  $d_C$ , is given by

$$d_C = \frac{fL}{\sqrt{L^2 + r^2} - f}, \quad (1)$$

where  $r$  is the radius of the circle on which the center of the lenses are located. One possible lens configuration is

$$\begin{aligned} \mathbf{P}_1^l &= (0, r, 0) \\ \mathbf{P}_2^l &= \left( \frac{\sqrt{3}r}{2}, \frac{-r}{2}, 0 \right) \\ \mathbf{P}_3^l &= \left( -\frac{\sqrt{3}r}{2}, \frac{-r}{2}, 0 \right). \end{aligned}$$

Finally, if the camera is perfectly aligned, the positions of the CCD centers for this lens configuration will be

$$\begin{aligned}\mathbf{P}_1^c &= \left(0, r \left(1 + \frac{d_c}{L}\right), -d_c\right) \\ \mathbf{P}_2^c &= \left(\frac{\sqrt{3}r}{2} \left(1 + \frac{d_c}{L}\right), -\frac{r}{2} \left(1 + \frac{d_c}{L}\right), -d_c\right) \\ \mathbf{P}_3^c &= \left(-\frac{\sqrt{3}r}{2} \left(1 + \frac{d_c}{L}\right), -\frac{r}{2} \left(1 + \frac{d_c}{L}\right), -d_c\right).\end{aligned}$$

The purpose of alignment and calibration is to compensate for the placement of the CCDs as to agree with the above equations. This is a critical step to ensure the accuracy of the measurements.

### *3D Coordinates and Sensitivity*

Suppose that a particle is at position  $(x, y, z)$ . Using geometric optics it is possible to find the pixel coordinates,  $\mathbf{I}_i$ , of the particle image on CCD  $i$ :

$$\begin{aligned}\mathbf{I}_1 &= \left(-x \frac{d_c}{Sz}, -(y - r_n) \frac{d_c}{Sz}\right) \\ \mathbf{I}_2 &= \left(-\left(x - \frac{\sqrt{3}}{2} r_n\right) \frac{d_c}{Sz}, -\left(y + \frac{r_n}{2}\right) \frac{d_c}{Sz}\right) \\ \mathbf{I}_3 &= \left(-\left(x + \frac{\sqrt{3}}{2} r_n\right) \frac{d_c}{Sz}, -\left(y + \frac{r_n}{2}\right) \frac{d_c}{Sz}\right),\end{aligned}$$

where

$$r_n = r \left(1 - \frac{z}{L}\right),$$

and where  $S$  is the pixel size. Using these coordinates, the side length,  $s$ , of the equilateral triangle formed by overlaying the three CCD images is given by

$$s = \frac{\sqrt{3} r_n}{Sz} d_c. \quad (2)$$

It is now easy to obtain the sensitivities of a 3DPTV camera:

$$\frac{d\mathbf{I}_{i,x}}{dx} = \frac{d\mathbf{I}_{i,y}}{dy} = -\frac{d_c}{Sz} \quad (3)$$

$$\frac{ds}{dz} = -\frac{\sqrt{3}r}{Sz^2} d_c. \quad (4)$$

The sensitivity in the  $x$ - and  $y$ -directions are the same; however, in most cases, the sensitivity in  $z$  is much lower, about 10 times. It is interesting to note that the ratio of these sensitivities

depends only on  $r$  and  $z$ ,

$$\frac{\frac{dI_{i,x}}{dx}}{\frac{ds}{dz}} = \frac{z}{\sqrt{3}r}.$$

Equations 1, 3 and 4 show that higher  $f$  leads to better accuracy. Of course,  $f$  is constrained by space limitations and by the need for sufficient depth of field. Increasing  $r$  increases the accuracy in  $z$  and decreases the accuracy in the other directions. Decreasing the distance between the camera and the test volume increases all the accuracies. However, a refractive index change along the light path, caused for example by the presence of a glass window or non-uniform surrounding medium, introduces a difficulty if  $r$  is not small compared to  $z$ . This difficulty is discussed further in the next paragraph. Finally, in most cases, decreasing  $L$  increases the accuracy. However, the blur radius range limitation does not allow us to reach the highest sensitivities.

### 3.2.2 Varying Media Influence

In most of the results presented here, a glass window has to be taken into account. Although the sensitivities are not significantly changed, the triangles are no longer equilateral. This poses an additional problem to the data processing program. To keep the triangles nearly equilateral, the light path from a particle to the CCD has to have a small angle of incidence at the glass. This leads to two important conditions. The first is that the camera has to look perpendicularly through the glass and the second is that the ratio  $r/z$  has to remain much less than 1.

### 3.2.3 Current Camera

The current camera is designed to investigate a  $50 \times 50 \times 50$  mm<sup>3</sup> test volume. The CCDs are UNIQ UP-1830-10 cameras. Each sensor is composed of  $1024 \times 1024$  px, each pixel is square with a side length of  $6.45 \mu\text{m}$ . Three 60 mm focal length lenses are placed at the corners of an equilateral triangle inscribed in a circle of radius of 42.5 mm. The CCDs are off-centered an additional 0.84 mm compared to the calculated values in the alignment section so that the entire CCD is used. This increases the number of pixels used by 58% relative to the setup without the offset. The target plate used for alignment was placed 625 mm from the camera. The  $z$ -range of the test volume is 517 mm to 567 mm from the camera.

Using all the results that were obtained before, the sensitivities in  $x$  and  $y$  range from 18.1 to 19.9 px/mm and the sensitivity in  $z$  ranges from 2.35 to 2.83 px/mm, within the test volume. The ratio of the sensitivities is therefore between 7.0 and 7.7.

### **3.3 Data Processing Program**

The data processing program was written to convert a set of three images into 3D positions and when required, computes a velocity field from those results.

The images are first Fourier transformed to remove noise inherent to the camera system. Next a smoothing filter blurs the image with a Gaussian blur. By doing this the blurred particles remain Gaussian and their centroid does not change. After the additional blurring the noise is greatly reduced. The final step is to scale the images, by matching the contrast of the three images.

After these image manipulations, the locations of the peaks on each image are searched for. The positions of the peaks are corrected by applying the calibration results. Using the three CCD images, triangles are formed from corresponding peaks. Three dimensional particle positions can then be calculated and particle tracking is performed between two successive frames.

The data processing program will be explained in more detail in a future publication [7].

### **3.4 Error Analysis**

Without a thorough understanding of the errors associated with 3DPTV, the results have very little meaning. It is therefore important to understand the many different types of errors. Because of this a thorough error analysis was performed, both theoretically and experimentally.

The first of these errors is the manufacturing error. This error takes into account all possible inaccuracies in the lens positions as well as inaccuracies in the physical construction of the calibration setup. These errors lead to an error estimation which is proportional to the measured velocities. The second error is due to the data processing program. Here, the error is constant for all velocities and depends mainly on the depth position of the particle. A thorough discussion of these errors is out of scope for this article but will be discussed in a future paper[8].

In addition to the errors of the 3DPTV system, other inaccuracies have to be considered. In a supersonic flow, changes of indices of refraction have to be considered when evaluating the 3D position of each particle. In addition, the finite size of particles is important wherever high velocity gradients exist. These inaccuracies will be discussed in this section.

#### **3.4.1 Index of Refraction**

The fluid inside and outside the test section is subject to change in its refractive index since the fluid density is not constant. The refractive index of air is roughly a linear function of

its density

$$n = 1 + K \frac{\rho}{\rho_{\text{ref}}},$$

where  $K = 0.000292$  and  $\rho_{\text{ref}} = 1.225 \text{ kg/m}^3$ . In the Ludwieg Tube facility, with an initial pressure of 100 kPa, the density could vary between  $0.15 \text{ kg/m}^3$  and  $1 \text{ kg/m}^3$  and therefore, the refractive index can vary between 1.00004 and 1.0002. The refractive index remains very close to 1 in all cases. It is also important to note, that even if the indices of refraction were constant they would not be known exactly, and hence would cause an error.

#### *Index of Refraction uncertainty*

The indices of refraction of the fluid and the glass are not known exactly; therefore, the actual particle location can not be calculated from the apparent particle location. Assuming we have three indices of refraction (*e. g.*, test-section gas, window, and outside air) and that the angles are small, the error,  $\epsilon$ , on the CCD due to uncertainties in the indices of refraction is given by

$$\frac{\epsilon}{h} = \frac{\left| \frac{n_3}{n_2} d_2 \left( \frac{\Delta n_3}{n_3} - \frac{\Delta n_2}{n_2} \right) + \frac{n_3}{n_1} d_1 \left( \frac{\Delta n_3}{n_3} - \frac{\Delta n_1}{n_1} \right) \right|}{d_3 + d_2 \frac{n_3}{n_2} + d_1 \frac{n_3}{n_1}},$$

where

$$h = \sqrt{h_x^2 + h_y^2},$$

$h_x$  and  $h_y$  being the  $x$ - and  $y$ -distances, respectively, from the lens center to the image location on the CCD.  $n_1$  and  $n_3$  are the indices of refraction of the fluid inside and outside of the test section, respectively, while  $n_2$  is the index of refraction of the glass.  $\Delta n_i$  is the uncertainty in the index of refraction  $n_i$ ,  $d_3$  is the distance from the camera to the glass,  $d_2$  is the thickness of the glass, and  $d_1$  is the distance from the glass to the particle.

#### *Finite Density Gradients*

In the test section of supersonic flow, significant finite density gradients will exist. These density gradients will cause a change in the index of refraction of the fluid. Assuming that the index of refraction of all three media are approximately equal, one can find the error in terms of the index of refraction gradient,  $\frac{dn}{y}$ . It is also assumed that the particle is at a distance  $z$  from the lens and that it is inside the density gradient, that the gradient is perpendicular to the light path, and that the light travels through the density gradient for a distance,  $L_g$ . The error,  $\epsilon$ , on the CCD is

$$\frac{\epsilon}{d_C} = \frac{dn}{y} \frac{L_g^2}{2z}.$$

#### *Infinite Density Gradients*

Shocks produce what can be considered infinite density gradients. As in the case of a finite density gradient, these density gradients create a change in the index of refraction of the

fluid. We will assume that the index of refraction is approximately constant everywhere, and that there is only a change in the index of refraction across the shock. The angle between the light path and the density gradient is  $\alpha$ . The distance from the particle to the shock is  $L_s$  and the distance from the particle to the lens is  $z$ . The error,  $\epsilon$ , on the CCD is then given by

$$\frac{\epsilon}{d_C} = \tan(\alpha) \frac{\Delta n}{n} \frac{L_s}{z}.$$

### 3.4.2 Tracking Error

A significant error in the 3DPTV system is not caused by the camera itself, but rather the ability of the seeding particles to accurately follow the flow. Because the particles have mass, they are unable to respond instantaneously to the flow. Most particles suitable for seeding supersonic flow have a specific weight near one.

The speed of a particle,  $U_p$ , in Stokes flow, across of shock with speed  $U_1$  before the shock, and speed  $U_2$  behind the shock is

$$U_p = U_2 + (U_1 - U_2) e^{-\frac{9\mu}{2\rho_s r_s^2} t}.$$

Therefore the time response across a shock is characterized by a time constant,  $\tau$ , which is defined as

$$\tau = \frac{2\rho_s r_s^2}{9\mu}.$$

As could be expected, the time constant depends only on the particle radius, the particle density, and the viscosity of the fluid. Given that the viscosity is fixed by the choice of flow conditions,  $r_s^2$  should be minimized. However, since the amount of light incident on the particle is proportional to  $r_s^2$ , this would also decreases the scattered light which is used to detect particles. The time constant also decreases with decreasing particle density.

Because of the momentum of the particles, the particles will form what can be considered as an apparent shock thickness. This shock thickness can be defined as the region around a shock where the velocity of the particle differs from the flow velocity by more than some percentage. Since between the two frames the particle moves some finite distance, 3DPTV is not a point measurement system. Rather, the velocity measurement is an integration of the velocity from start to finish. Because of this, it is not clear where the velocity vector should be placed; therefore, the current authors chose to place the velocity vector at the midpoint of the start and end positions. This placement becomes particularly important when examining the velocity error around a shock. For Stokes flow, there is an analytic solution for the apparent shock thickness for a given velocity tolerance. Figure 9 shows the relationship between the shock thickness and the velocity tolerance. There are three distinct cases that need to be considered. The first case is where a particle starts upstream of the shock and finishes downstream of the shock, but the midpoint between the start and end positions is upstream of the shock, this case forms the curve left of the first dashed line.

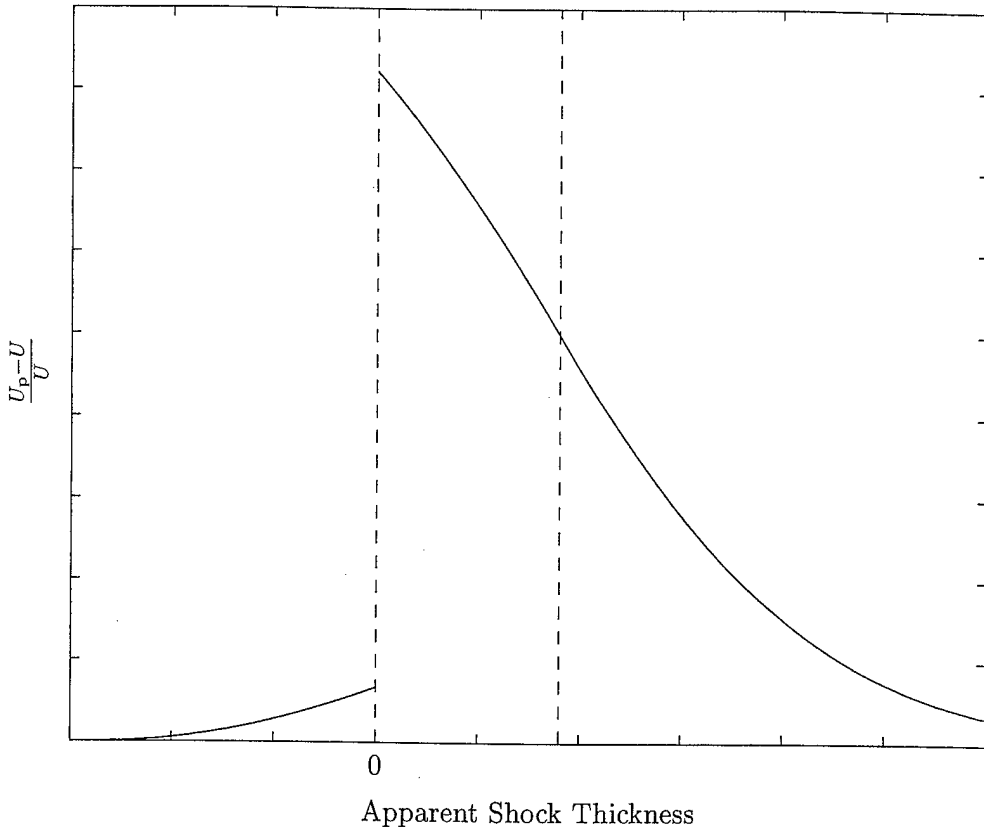


Figure 9: Apparent shock thickness due to finite mass of particles.

The second case is similar to the first case, except that the midpoint between the start and end positions is downstream of the shock, and this case forms the curve between the two dashed lines. The final case is when the start and end positions of a particle are both downstream of the shock, and forms the remainder of the curve. The theory supposes that the particle follows the flow perfectly upstream of the shock. We can see from the figure that the upstream apparent shock thickness is small compared to the downstream thickness when the time duration between frames is of the order of the time constant. Because of this, it is reasonable to consider the downstream thickness as the total shock thickness. The downstream shock thickness,  $\delta_s$ , is given by

$$\frac{\delta_s}{U_2 \tau} = \bar{U} - \frac{\bar{t}\epsilon}{e^{\bar{t}} - 1} - \frac{\bar{t}}{2}(1 + \epsilon) + \ln\left(\frac{(e^{\bar{t}} - 1)\bar{U}}{\bar{t}\epsilon}\right),$$

where  $\bar{U} = \frac{U_1}{U_2} - 1$ ,  $\bar{t} = \frac{t_s}{\tau}$ ,  $t_s$  being the time between frames, and  $\epsilon$  is the velocity ratio,  $\frac{U_p - U}{U}$ , used to define the shock thickness with  $U$  being the velocity of the flow.

#### *Discretization Error*

Part of the error in peak searching is due to discretization error. A theoretical approximation

for the discretization error, for  $r_b > 1$ , shows that the error,  $\epsilon$ , is

$$\epsilon \propto \frac{1}{Ar_b}, \quad (5)$$

where  $A$  is the amplitude of a particle image on the CCD. For a given particle brightness the product  $Ar_b^2$  is constant. Therefore for a constant particle brightness the error is proportional to the blur radius. The constant of proportionality is best found by numerical simulations for a particular peak searching algorithm.

### *CCD Noise Error*

A theoretical approximation for the error due to noise on the CCD,  $\epsilon$ , can be found. It proves that, for  $r_b > 1$ , the error is

$$\epsilon \propto \frac{E}{A}, \quad (6)$$

where  $E$  is the amplitude of the noise. For a constant particle brightness the error is proportional to the blur radius squared. Once again, the constant of proportionality can be found by numerical simulations.

## 3.5 Results

In this section, several results will be presented. The first of these are theoretical results to examine the highest accuracy that can be obtained using the program. A moving plate is then examined to determine the errors one can get on displacements and positions. A slightly less serious but quite impressive result is then presented, which shows, using a doll face how well a surface can be represented in a single measurement. Finally, a supersonic flow result will be presented.

### 3.5.1 Synthetic Images

An important test of the 3DPTV system was the processing of synthetic images. These images allow for a complete testing of the program, including triangle formation and triangulation calculations.

The domain was divided into 21 planes perpendicular to the camera axis. In each of these planes, 400 particles were created and their images were added to form the synthetic images. Therefore, each synthetic image contained 8,400 particle images. Each particle image was Gaussian blurred with a 10% blur radius of approximately 3 px. A total of 100 sets of images were created and then processed. In each of the planes, the results were averaged to evaluate the errors (*i. e.*, each symbol on Figures 10 and 11 represents an average of 40,000 results).

As expected, the mean error tends to zero. In each of the planes, the mean error is lower than 0.009  $\mu\text{m}$  and 0.09  $\mu\text{m}$  in the  $x$ - and  $y$ -directions and in the  $z$ -direction, respectively.

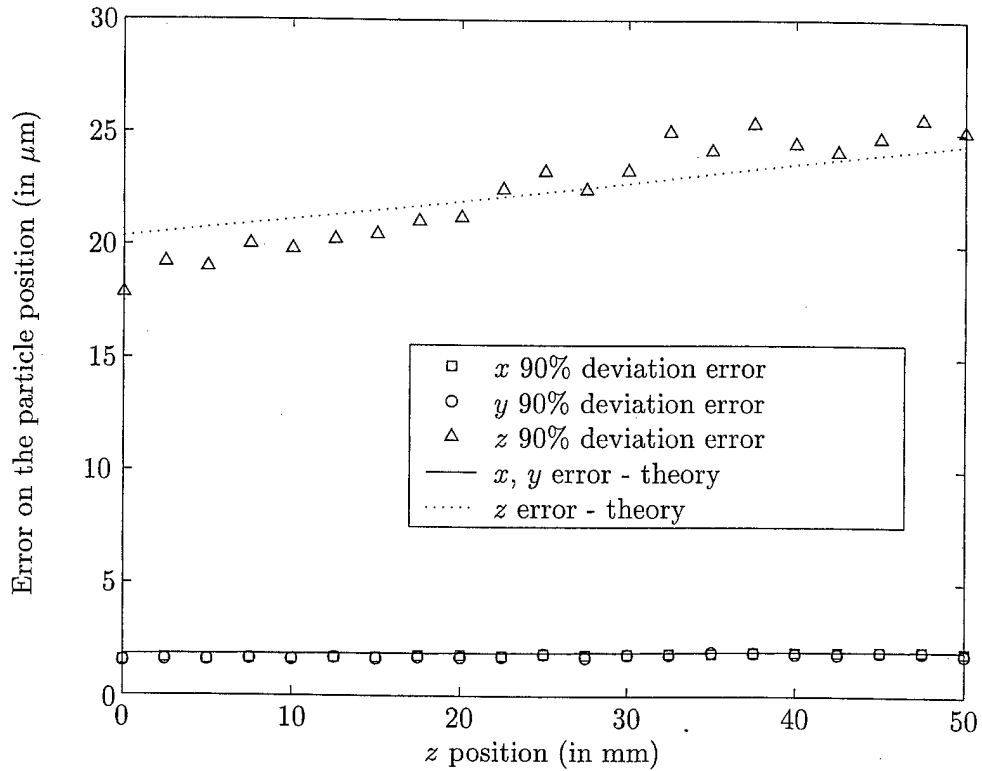


Figure 10: 90% deviation error of particle positions from synthetic images

The 90% deviation error was also evaluated and is shown in Figure 10. As expected, this error varies according to theory [8].

The ratio of the 90% deviation errors was also evaluated, as is shown in Figure 11, and shows a very good agreement with the trend line obtained theoretically [8].

### 3.5.2 Moving Plate

The moving plate test case was performed using a flat plate with an array of white dots on a black background. There were 100 dots per square inch. The plate was placed at  $z$ -positions of 469, 494, 519, 529, 539, 549, 559, 569, 594, and 619 mm from the camera. The plate was then moved in three equal increments of 2.54 mm in the  $y$ -direction for each of the  $z$ -locations, this resulted in a total of 6 displacement vectors for each  $z$ -position (3 displacements of 2.54 mm, 2 displacements of 5.08 mm and 1 displacement of 7.62 mm). Similarly the plate was moved in three equal increments of 2.54 mm in the  $z$ -direction for each  $z$ -position.

First, the mean error was evaluated. This error is proportional to the displacement. Figure 12 shows the relative mean error obtained for 2.54 mm and 5.08 mm displacements, each data point is an average of 3 and 2 values, respectively. In this plot, the 7.62 mm results are not

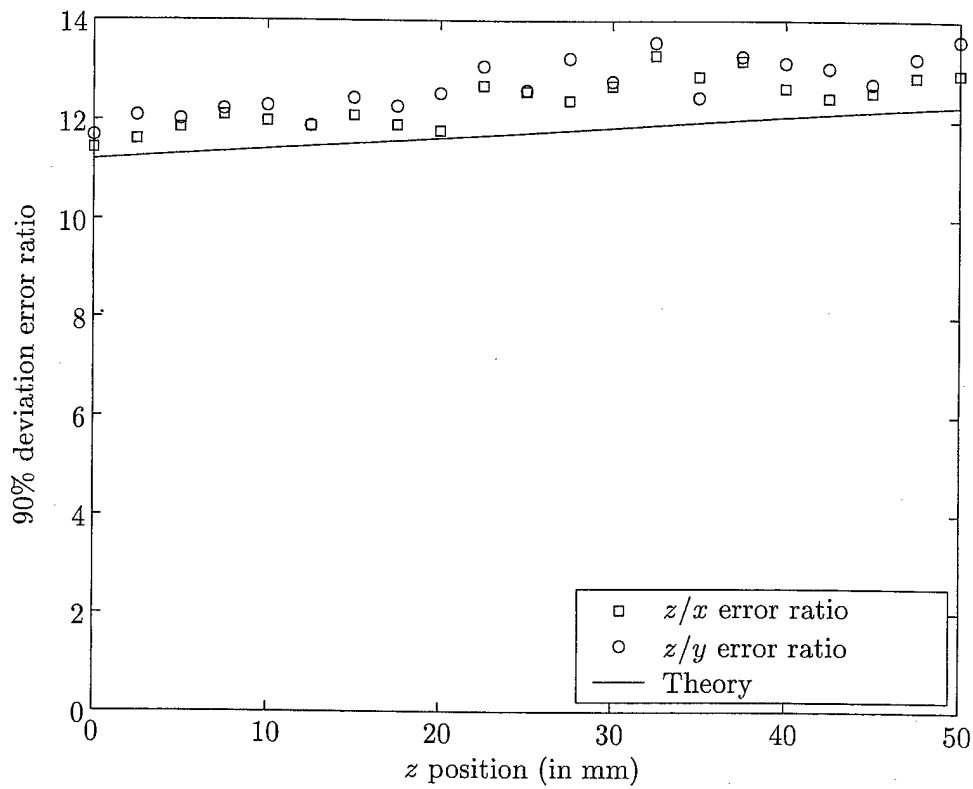


Figure 11: Ratio of the 90% deviation error of particle positions from synthetic images.

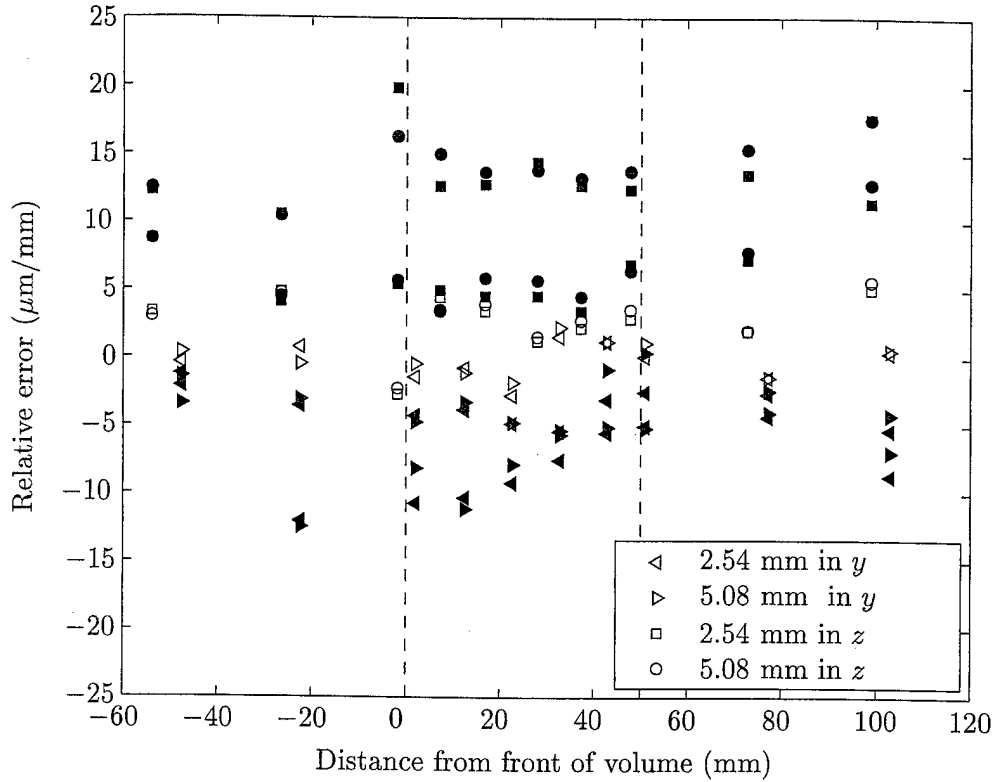


Figure 12: Mean plate displacement error. White, grey, and black symbols refer to the errors in the  $x$ -,  $y$ -, and  $z$ -directions respectively. The 2.54 mm and the 5.08 mm cases are the average of 3 and 2 data points, respectively.

shown since they correspond to the average of the three 2.54 mm results.

Even though the mean errors are very small, all within 2%, they remain in general far above the results expected theoretically [8]. One possible reason for the inaccuracies of the  $y$ -measurement in the  $z$ -displacement case, is that the whole camera was moved instead of the plate. Due to the weight of the camera and the lack of robustness of the  $\mu\text{m}$  stages, it might have changed its pitch angle very slightly when moved. An inaccuracy of  $20 \mu\text{m}$  per mm in the  $y$ -measurement can be obtained by having a change in pitch angle of less than  $5 \times 10^{-5} \text{ rad per mm}$  (less than  $0.003^\circ$  per mm). Furthermore, the resolution of the gauges that measured the displacements is  $25.4 \mu\text{m}$ , it is possible that part of the error comes from inaccuracies in the displacement of the plate.

The 90% deviation error of the displacements was also evaluated. The results are plotted in Figure 13. Each symbol is the average of the 90% deviation errors from three and two data sets in the 2.54 mm and the 5.08 mm cases, respectively.

As expected from theory, the error can be separated into two parts. The first of these is proportional to the displacement and the second is constant for all displacements. The total

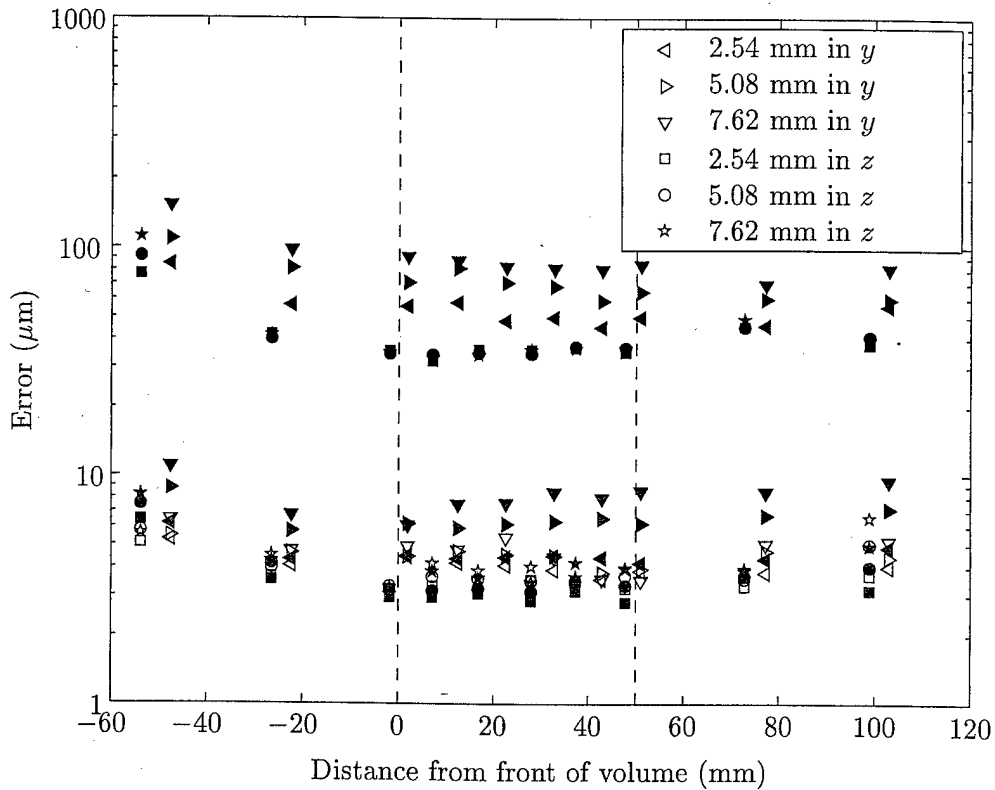


Figure 13: 90% deviation errors of plate displacement. White, grey, and black symbols refer to the errors in the  $x$ -,  $y$ -, and  $z$ -directions respectively. The 2.54 mm and the 5.08 mm cases are the average of 3 and 2 data points, respectively.

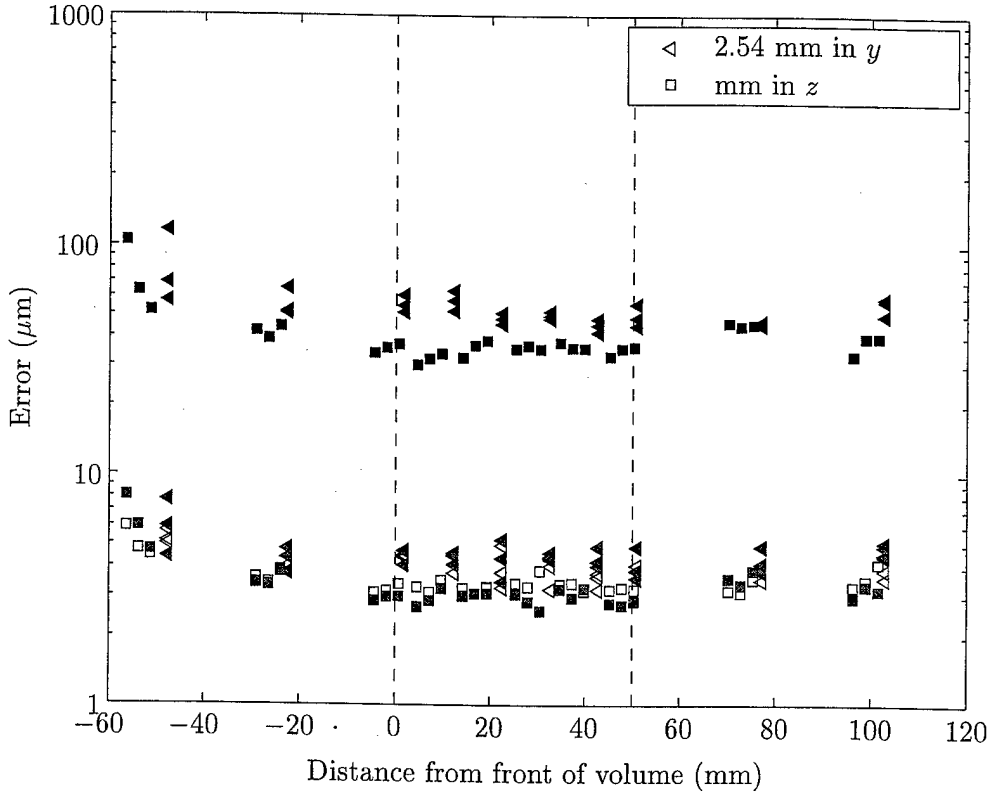


Figure 14: 90% deviation errors of plate displacements. White, grey, and black symbols refer to the errors in the  $x$ -,  $y$ -, and  $z$ -directions, respectively.

90% deviation error,  $\delta D$ , can therefore be written as

$$\delta D = \sqrt{C_1^2 D^2 + C_2^2}. \quad (7)$$

Since, for most flow measurements, the displacement of the particles will be smaller than 2.54 mm, it is interesting to analyze the results for this particular displacement, as this represents the worst case scenario. Figure 14 therefore gives a higher bound for the 90% deviation error one can expect with the 3DPTV setup.

According to these results, the 90% deviation error in the test volume remains under  $5.2\mu\text{m}$  and under  $63\mu\text{m}$  in the  $x$ -,  $y$ -directions and in the  $z$ -direction, respectively.

Both the theoretical values and the experimental data of the 90% displacement error are shown in Figure 15. The discrepancy in the results for low  $z$ -position comes from the fact that the dots on the plate appear very blurred and that the amplitude of the peaks becomes very low. This effect is presented in Equations 5 and 6.

The varying part of the 90% deviation error is presented in Figure 16. Although these errors remain quite small ( $1\mu\text{m}$  per mm in  $x$  or  $y$  and  $10\mu\text{m}$  per mm in  $z$ ), they are much higher than what was expected. A possible reason for that is again the lack of robustness of the

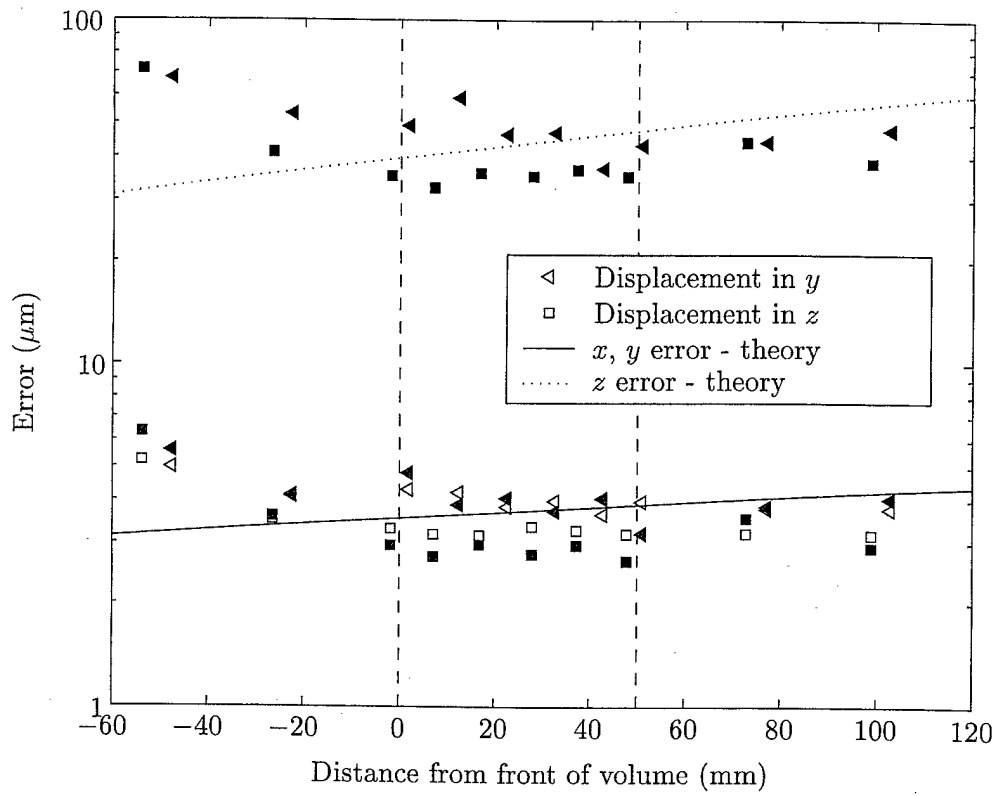


Figure 15: Fixed part of 90% deviation errors of plate displacements. White, grey, and black symbols refer to the errors in the  $x$ -,  $y$ -, and  $z$ -directions, respectively.

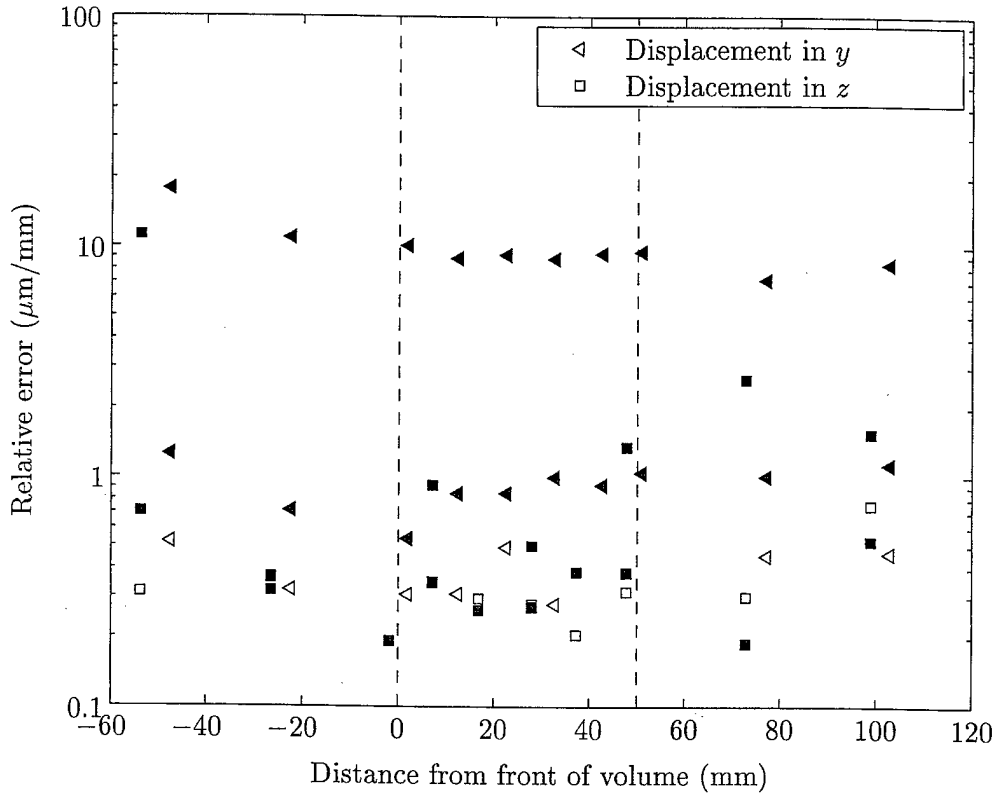


Figure 16: Variable part of 90% deviation errors of plate displacements. White, grey, and black symbols refer to the errors in the  $x$ -,  $y$ -, and  $z$ -directions, respectively.

translation stages. In fact, if during the movement of the plate in the  $y$ -direction, its pitch angle changed by only  $4.5 \times 10^{-4}$  rad per mm ( $0.026^\circ$  per mm), the 90% deviation in  $z$  would reach  $10 \mu\text{m}$ . A small roll angle of  $4.5 \times 10^{-5}$  rad per mm ( $0.0026^\circ$  per mm) is sufficient to explain the inaccuracies in  $x$  and  $y$ .

From all the results presented here, it is possible to obtain an upper bound for the velocity errors. The mean errors will be approximately

$$|\Delta U_x| = \sqrt{24U_x^2 + 0.15U_y^2 + 206U_z^2} \times 10^{-3} \quad (8)$$

$$|\Delta U_y| = \sqrt{0.15U_x^2 + 24U_y^2 + 206U_z^2} \times 10^{-3} \quad (9)$$

$$|\Delta U_z| = \sqrt{54U_x^2 + 54U_y^2 + 25U_z^2} \times 10^{-3}, \quad (10)$$

whereas an estimation of 90% deviation errors of the velocities is

$$\delta U_x = \sqrt{75U_x^2 + 12U_y^2 + 9U_z^2 + \frac{15 \times 10^{-4}}{t_s^2}} \times 10^{-4} \quad (11)$$

$$\delta U_y = \sqrt{12U_x^2 + 75U_y^2 + 9U_z^2 + \frac{15 \times 10^{-4}}{t_s^2}} \times 10^{-4} \quad (12)$$

$$\delta U_z = \sqrt{87U_x^2 + 87U_y^2 + 0.85U_z^2 + \frac{23 \times 10^{-4}}{t_s^2}} \times 10^{-3} \quad (13)$$

where the velocities and the time between frame,  $t_s$ , are in m/s and in s, respectively.

If in fact, most of the disagreement with theory is due to the inaccuracy of the plate placement, these errors could be much smaller. Since the purpose of the present work is not to find the exact accuracy of the system and that, due to inertia, the actual error will depend most heavily on the particles ability to track the flow, Equations 8 through 13 are only an estimate of the velocimetry errors.

### 3.5.3 3D Solid Imaging

An additional capability of the 3DPTV system is the ability to do 3D solid imaging. To illustrate this capability the system was used to image the face of a doll. This was done by painting a doll face black, and putting a large number of white dots on the face. While it is hard to make analytic conclusions from the results, Figure 17 shows excellent resolution of the face. Some of the roughness on the image is possibly due to the fact that some of the white dots were large and non-circular. Note that these results were obtained using an old version camera, which did not take advantage of offsets. This camera was able to investigate a  $10 \times 10 \times 10 \text{ cm}^3$  volume but with a lower accuracy.

### 3.5.4 Sonic Jet Injection

The ultimate goal of the current authors is to use the 3DPTV system to image supersonic flows. Particle tracking measurements in supersonic flows are particularly challenging and present many problems not seen in slower flows. The primary problem is that in order for the particles to respond quickly to the flow they must be very small.

Experiments using a sonic jet injector with  $1 \mu\text{m}$  diameter olive oil droplets were conducted. Even with a 200 mJ Nd:YAG laser these particles were very dim and detection was very difficult. Despite the low signal to noise ratio the 3DPTV system was able to produce an accurate velocity field. Figure 18 shows an instantaneous velocity field containing 224 vectors, which is approximately 35 vectors per cubic centimeter. The particles were accelerated to sonic speeds through a converging nozzle with an outlet diameter of 7 mm. The region

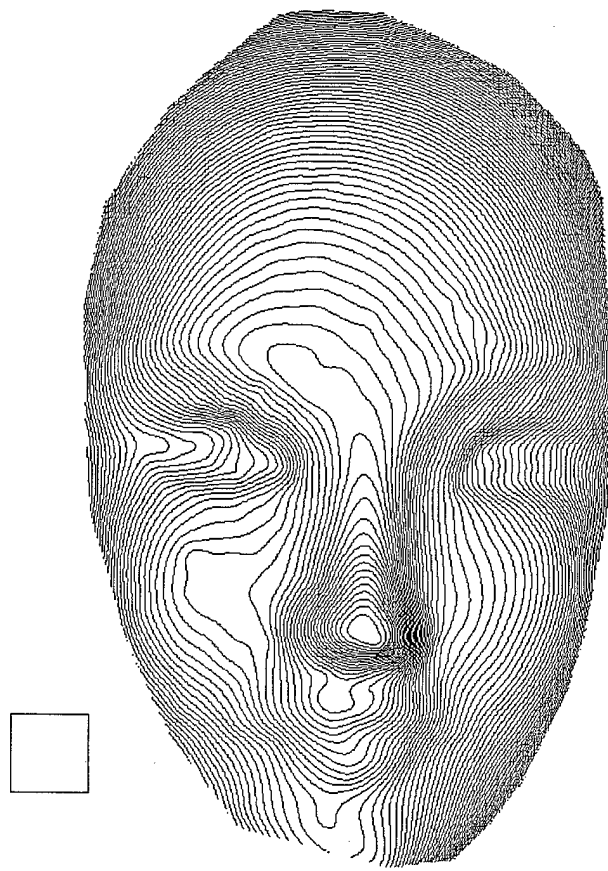


Figure 17: Three dimensional solid imaging of a doll face. The square has a side length of 1 cm. These results were taken with an older version camera having less accuracy but able to image a  $10 \times 10 \times 10$  cm<sup>3</sup> volume.

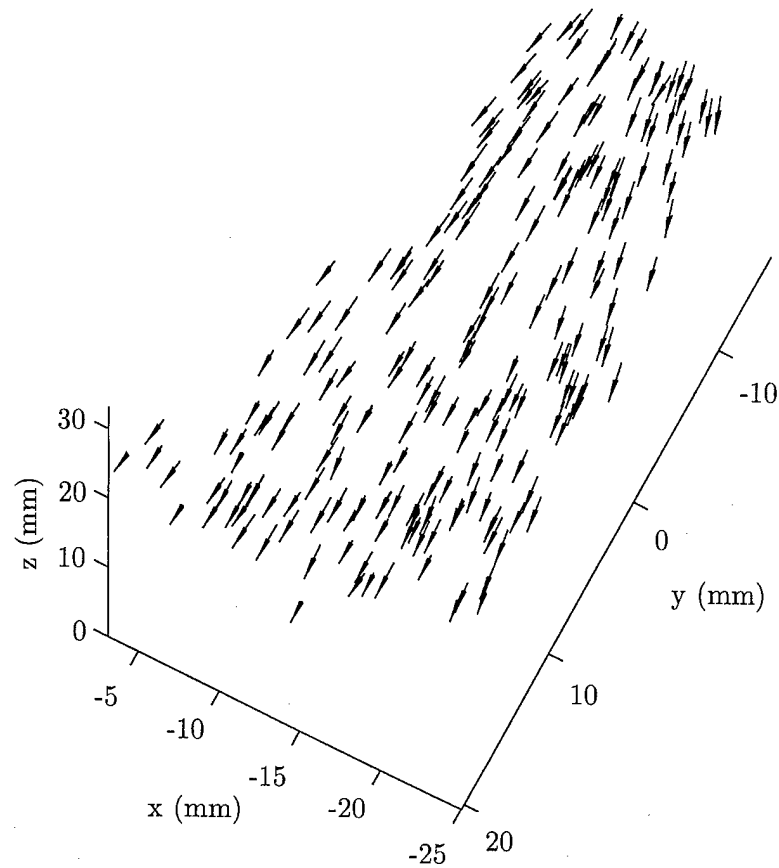


Figure 18: Velocity vectors of a sonic jet injector with  $1 \mu\text{m}$  olive oil seeding particles.

downstream of the injector nozzle was kept in vacuum; therefore, the particles continued to accelerate to supersonic speeds after exiting the injector.

### 3.6 Conclusions

The 3DPTV system has been shown to have excellent accuracy. For velocities parallel to the camera face the accuracy is within 0.25% and for velocities perpendicular to the camera face the accuracy is within 2.5%. These errors are well understood and agree with the theoretical estimates. Solid surface imaging of a doll face provided impressive, albeit non-quantitative results. Most importantly, velocity measurements of a sonic jet were made. These results are promising, although the vector density is lower than desired. Future work has begun on using larger and lighter particles, which will significantly improve the luminosity of the

particles. With brighter particles the results should begin to approach that of the synthetic images and flow fields with over 5,000 vectors should be obtainable.

## 4 General Conclusions

The supersonic Ludwieg Tube at GALCIT was completed and taken into operation. The injection Ludwieg Tube was constructed and taken into operation, thus completing a compact, inexpensive supersonic injection facility. The implementation of three-component, three-dimensional particle image velocimetry in supersonic air flows from the instrument existing for low speed water flows at the time of inception of the program required a much greater development effort than had been anticipated at the outset. Major redesign of the hardware and new software development as well as experimentation with particle-generating systems produced an instrument that is now able to fulfill the tasks demanded of it for the project with good accuracy and spatial resolution.

## 5 Personnel associated with the research

1. Hans G. Hornung (PI), Kelly Johnson Professor of Aeronautics
2. Nicholas Ponchaut, Graduate Research Assistant
3. Christopher Mouton, Graduate Research Assistant
4. Bahram Valiferdowsi, Staff Engineer

## 6 Publications resulting from the work

M. Y. El-Naggar, J. T. Klamo, M.-H. Tan, and H. G. Hornung. Experimental verification of the mach-number field in a supersonic ludwieg tube. Submitted to: *AIAA Journal*, 2004.

C. A. Mouton, N. F. Ponchaut, and H. G. Hornung. Full three dimensional particle triangulation velocimetry and applications. Submitted to: *Measurement Science and Technology*, 2003.

N. F. Ponchaut, C. A. Mouton, and H. G. Hornung. Accuracy and verification of the 3D particle triangulation velocimetry system. Submitted to: *Measurement Science and Technology*, 2003.

## 7 Honors and awards

H. G. Hornung:

Fellow, AIAA (2003); Fellow, Royal Aeronautical Society (2001); Ludwig Prandtl-Ring (1999); National Academy of Engineering (1997); Royal Swedish Academy of Engineering Sciences (1991).

N. Ponchaut:

Rolf Buehler Prize, GALCIT, 2000

## 8 Acknowledgments

The authors would like to thank Bahram Valiferdowsi for his generous and invaluable assistance in the design and implementation of this research. The Ludwig Tube is operated using funds from AFOSR under the supervision of Dr. J. Schmisseur. Christopher Mouton's studies are funded by the National Defense Science and Engineering Grant.

## References

- [1] M. Y. El-Naggar, J. T. Klamo, M.-H. Tan, and H. G. Hornung. Experimental verification of the mach-number field in a supersonic ludwig tube. Submitted to: *AIAA Journal*, 2004.
- [2] C. E. Willert and M. Gharib. Three-dimensional particle imaging with a single camera. *Experiments in Fluids*, 12:353–358, 1992.
- [3] H.-G. Maas, A. Gruen, and D. Papantoniou. Particle tracking velocimetry in three-dimensional flows. *Experiments in Fluids*, 15:133–146, 1993.
- [4] F. Pereira, M. Gharib, D. Dabiri, and D. Modarress. Defocusing digital particle image velocimetry: a 3-component 3-dimensional DPIV measurement technique. application to bubbly flows. *Experiments in Fluids*, Supplement:S78–S84, 2000.
- [5] R. N. Kieft, K. R. A. M. Schreel, G. A. J. van der Plas, and C. C. M. Rindt. The application of a 3D PTV algorithm to a mixed convection flow. *Experiments in Fluids*, 33:603–611, 2002.
- [6] F. Pereira and M. Gharib. Defocusing digital particle image velocimetry and the three-dimensional characterization of two-phase flows. *Measurement Science and Technology*, 13:683–694, 2002.

- [7] C. A. Mouton, N. F. Ponchaut, and H. G. Hornung. Full three dimensional particle triangulation velocimetry and applications. Submitted to: *Measurement Science and Technology*, 2003.
- [8] N. F. Ponchaut, C. A. Mouton, and H. G. Hornung. Accuracy and verification of the 3D particle triangulation velocimetry system. Submitted to: *Measurement Science and Technology*, 2003.

## **APPENDIX**

### **Original Statement of Work**

Year 1.:

1. Design and construct the injection system. This consists of the injection Ludwieg tube (ILT) leading to the injection nozzle in the test section via a quick-acting valve. Design and construct the injection wall, for generating a new, laminar boundary layer upstream of the injection point.
2. Shake down the ILT and its synchronized operation with the LT. Test out parameter range limits using schlieren visualization.
3. Design and construct the DDPIV system, including suitable optical access to the test section, purchase and construction of triple camera, purchase and assembly of computers and frame grabbers, installation of software.
4. Test and calibrate the complete system, shake down and find limits of spatial resolution and flow parameter ranges.

Years 2 and 3:

1. In consultation with the computational fluid dynamics community, define the test cases of particular interest and concentrate initial efforts on those, in order to establish a rapport with the computational groups.
2. Explore the parameter space (Reynolds number, momentum ratio, oncoming boundary layer state, injection Mach number, density ratio) in order to discover where qualitative changes occur. Delineate the boundaries on a map of parameter space.
3. Build database of detailed flow field measurements in specific regions of the parameter space.
4. Document results in easily accessible electronic form and make them openly available to researchers approved by the AFOSR.
5. Document results in publications